Polymer Testing 151 (2025) 108963

Contents lists available at ScienceDirect

Polymer Testing

journal homepage: www.elsevier.com/locate/polytest

Synergistic integration of porous polymer networks with solid-solid phase change material and surface-modified BN for enhanced thermal conductivity and latent heat storage

Minsu Kim [a], Dabin Park [c], Jooheon Kim [a,b,*]

[a] Department of Chemical Engineering, Chung-Ang University, Seoul, 06974, Republic of Korea
[b] Department of Intelligent Energy and Industry, Graduate School, Chung-Ang University, Seoul, 06974, Republic of Korea
[c] Department of Mechanical and Aerospace Engineering, University of California, Irvine, CA, 92679, USA

ARTICLE INFO

Keywords:
Solid–solid phase change material
Polyacrylamide
2-Amino-2-methyl-1,3-propanediol
Thermal conductivity
Thermal energy storage

ABSTRACT

Conventional phase change materials (PCMs) face two persistent challenges: low thermal conductivity and leakage during phase transitions. Studies have partially addressed these issues using porous carbon supports and core–shell encapsulation. However, these strategies often remain impractical for electronic thermal management applications due to their electrical conductivity or incompatibility with polymer matrices. Therefore, this study aims to develop a fundamentally new strategy that synergistically integrates a reinforced porous polyacrylamide–starch (PAM–S) framework, surface-functionalized agglomerated boron nitride (PA-ABN), and a Bi–Sn–In liquid metal alloy. The starch-modified PAM network enhanced structural integrity and inhibited filler sedimentation, facilitating a uniform filler distribution of the PA-ABN. Surface modification of ABN with polysilazane–silane improved polymer–filler interfacial adhesion and promoted the formation of a continuous, planar, through-plane thermal network, resulting in a higher thermal conductivity (3.34 W/m•K) than the unmodified ABN composites. Similarly, the well-integrated filler network and reinforced porous framework significantly enhanced mechanical robustness, increasing tensile strength from 2.16 MPa (original PAM) to 14 MPa. The Bi–Sn–In alloy, characterized by high thermal conductivity and a low melting point (62 °C), infiltrated the polymer matrix–filler micropores, further reducing the interfacial thermal resistance. This design led to a composite with a latent heat capacity of 138 J/g and excellent leakage resistance up to 120 °C, maintaining stable thermal performance over 100 cycles and demonstrating superior CPU cooling efficiency compared to conventional thermal interface materials. These findings demonstrate a novel PCM composite architecture that simultaneously achieves leakage control, durability, and high heat-transfer efficiency, making it suitable for advanced thermal management applications.

1. Introduction

Phase-change materials (PCMs) have gained significant attention for their ability to absorb, store, and release thermal energy during phase transitions [1–3]. This unique property makes them highly suitable for various thermal management applications, including energy storage systems [4,5], building temperature control [6,7], electronics cooling [8,9], and thermal protection in aerospace and textile industries [10,11]. Despite their advantages, conventional PCMs exhibit inherent limitations, such as low thermal conductivity and leakage during phase transitions, necessitating innovative strategies to enhance their practical applicability. During the solid-to-liquid phase change, fluid leakage remains a problem that must be addressed. Yan et al. used expanded graphite to address the leakage problem of polyethylene glycol, achieving a thermal conductivity of 2.48 W/m•K and latent heat of 161.4 J/g [12]. When the PCM enters the porous structure of expanded graphite, it remains confined within the pores during the solid-to-liquid phase transition, thereby preventing external leakage. However, while expanded graphite effectively prevents PCM leakage due to its porous structure, its high electrical conductivity limits its application in electronic devices. An alternative approach to addressing leakage involves fabricating core–shell structures. For example, Rajamony et al. fabricated organic/silver–coconut shell biochar composites that prevent leakage and exhibit high reliability under repeated thermal cycling [13]

* Corresponding author. Department of Chemical Engineering, Chung-Ang University, Seoul, 06974, Republic of Korea.
E-mail address: jooheonkim@cau.ac.kr (J. Kim).

https://doi.org/10.1016/j.polymertesting.2025.108963
Received 23 June 2025; Received in revised form 15 August 2025; Accepted 26 August 2025
Available online 27 August 2025
0142-9418/© 2025 The Authors. Published by Elsevier Ltd. This is an open access article under the CC BY-NC-ND license (http://creativecommons.org/licenses/by-nc-nd/4.0/).

PCMs are generally classified into organic, inorganic, and eutectic types. Organic PCMs, such as paraffin wax and fatty acids, are widely used because of their desirable properties, including chemical stability, non-corrosiveness, and recyclability over multiple thermal cycles. A notable example is 2-amino-2-methyl-1,3-propanediol (AMP), exhibiting a high latent heat storage capacity and undergoes solid–solid phase transition [14]. AMP has attracted increasing attention in PCM composite development due to its ability to improve both thermal performance and safety. AMP undergoes a solid–solid phase transition at 90 °C with a high latent heat of 230 J/g. This combination of high latent heat and solid–solid phase transition differentiates it from other organic PCMs, which typically exhibit solid–liquid phase transitions, enabling it to address leakage issues. In high-power electronic devices, such as CPUs, heat generation causes temperature increase, making the integration of heat-dissipating materials and PCMs essential for semiconductor protection. Conventional organic PCMs undergo a solid–liquid phase transition and exhibit high latent heat, necessitating strategies to address leakage issues. In contrast, AMP maintains high latent heat without leakage, requiring the use of a porous structure only when operating at temperatures above its melting point. However, its relatively low thermal conductivity limits its applications, necessitating the use of thermally conductive fillers or structural modifications to improve heat dissipation. Despite their high latent heat storage capacity, most organic and solid–solid PCMs inherently exhibit low thermal conductivity, typically below 0.5 W/m•K, which limits their effectiveness in rapid heat dissipation applications. To address this, thermally conductive fillers such as expanded graphite, carbon-based nanomaterials, and ceramic particles have been incorporated into PCM matrices. While these fillers can significantly enhance thermal conductivity, they generally occupy a portion of the PCM volume, leading to a reduction in the latent heat capacity. This trade-off between thermal conductivity and latent heat storage is a well-known challenge in PCM composite design, particularly when high filler loadings are required to achieve target heat transfer performance. Furthermore, excessive filler addition can disrupt the crystallization of PCM molecules, further reducing the phase change enthalpy and in some cases causing non-uniform melting/solidification behavior. Therefore, advanced composite architectures that enable efficient heat conduction pathways without severely compromising the latent heat content are essential for next-generation PCM-based thermal management systems.

To address these limitations, strategies for integrating PCMs into porous support matrices have been investigated, stabilizing the PCMs while enhancing their thermal conductivity and mechanical properties [15,16]. Polyacrylamide (PAM), a hydrophilic polymer, is widely used in applications such as water treatment, biomedical materials, adhesives, and superabsorbent gels due to its excellent mechanical strength and high-water retention capacity [17]. However, porous PAM primarily exists in hydrogel form, limiting its application as a thermal interface material (TIM) in electronic devices due to the water content. Therefore, this study aims to develop PAM-based composites by introducing thermal fillers into the pores formed during hydrogel synthesis and removing water through evaporation during polymerization. Additionally, in thermal management applications, these PAM-based porous structures are designed to effectively prevent PCM leakage while preserving structural integrity. Modifying PAM with starch produces a reinforced porous framework that enhances mechanical durability and viscosity, enabling uniform filler distribution within the composite [18]. Another effective strategy for improving the thermal performance of PCM composites involves incorporating high-thermal-conductivity materials. Recently, liquid metal-based materials, such as Bi–Sn–In alloys, have emerged as promising candidates due to their excellent heat-transfer properties and ability to infiltrate and fill interfacial pores. Chen et al. fabricated Bi–Sn–In alloy/Ag/Cu foam composite for thermal storage and management applications [19]. These alloys exhibit excellent wettability and low melting points, enabling them to form an efficient thermal interface within the composite structure. Similarly, Ki et al. fabricated a gallium/porous Cu composite to improve thermal regulation performance during repeated thermal cycling [20]. However, despite these favorable properties, achieving uniform dispersion of liquid metals within polymer matrices remains a significant challenge due to their high density and tendency to segregate.

Therefore, this study aims to develop a novel strategy for integrating a Bi–Sn–In liquid metal particles and polysilazane (PSZ)-coated, silane-modified aggregated boron nitride (PA-ABN) fillers into porous PAM–-starch (PAM–S)/AMP composites. ABN, a cluster of boron nitride (BN) particles, addresses the anisotropic thermal conductivity observed in plate-shaped hexagonal-BN (h-BN). However, ABN exhibits strong physical agglomeration and inherently low compatibility with polymer matrices. To address this limitation, the ABN surface was coated with PSZ and a silane coupling agent to improve its compatibility with the polymer matrix, thereby improving filler dispersion and interfacial adhesion while reducing pore formation caused by filler positioning within the matrix compared to pure ABN-based composites. Additionally, a small amount of liquid metal alloy was added, melting during the formation of the PAM–S matrix. It was mixed with the PA–ABN filler to reduce pore formation at the matrix–filler interface and slightly improve thermal conductivity. The combined effects of the porous PAM framework, AMP reinforcement, and liquid metal integration could result in composites with enhanced thermal conductivity, mechanical strength, and PCM leakage prevention, offering promising potential for next-generation thermal management systems.

2. Results and discussion

2.1. Thermal property evaluation of Bi–Sn–In alloys and surface modification of aggregated boron nitride

Fig. 1 illustrates the schematic fabrication process of the PA-ABN filler and the PAM–S/AMP/PA-ABN composite containing Bi–Sn–In alloy particles. The Supporting Information presents the detailed experimental procedures. Fig. 2(a) shows the DSC curve of the Bi–Sn–In alloy, exhibiting a melting point of 62 °C with a latent heat of 30.16 J/g. The Bi–Sn–In alloy, despite its low latent heat value for use as a PCM in a composite with a porous structure, exhibited higher thermal conductivity than most organic PCMs. In its liquid metal state, the alloy effectively filled the matrix–filler interface without leakage. The measured thermal conductivity of the Bi–Sn–In alloy was 28.4 W/m•K, confirming its high thermal conductivity. However, owing to the challenge of weighing bulk Bi–Sn–In alloy in quantities <1 g for incorporation into the composites, a size reduction process was necessary. The alloy was converted into small particles using a micropipette tip heated to approximately 60 °C.

ABN was surface-treated with PSZ and the APTES silane coupling agent to form PA-ABN. Surface modification of BN is typically challenging due to the need for physical processes, such as tip sonication or ball milling, to facilitate the attachment of functional groups to its surface [21,22]. However, for ABN (Fig. 2(b)), the BN particles exhibited a strong tendency to aggregate, and tip sonication or ball milling posed a risk of damaging the particles. In this study, the ABN surface was modified by simultaneously applying PSZ and a silane coupling agent. Following treatment, the Field-emission scanning electron microscopy (FE-SEM) imaging confirmed that PSZ uniformly coated the ABN surface (Fig. 2(c)).

The PA-ABN surface chemical structure was comprehensively investigated through deconvolution of the C 1s and Si 2p XPS spectra (Fig. 2(d & e)). In the C 1s spectrum, characteristic peaks were observed at 284.0 eV, 284.8 eV, 286.0 eV, 286.6 eV, and 288.9 eV, corresponding to the C–Si, C–C, C–N, C–O, and C=O bonding states, respectively [23]. The Si 2p spectrum revealed peaks at 102.5 eV, 101.7 eV, and 100.8 eV, corresponding to Si–C, Si–N, and Si–O bonds, respectively, confirming surface functionalization of the ABN particles [23]. Additionally, the

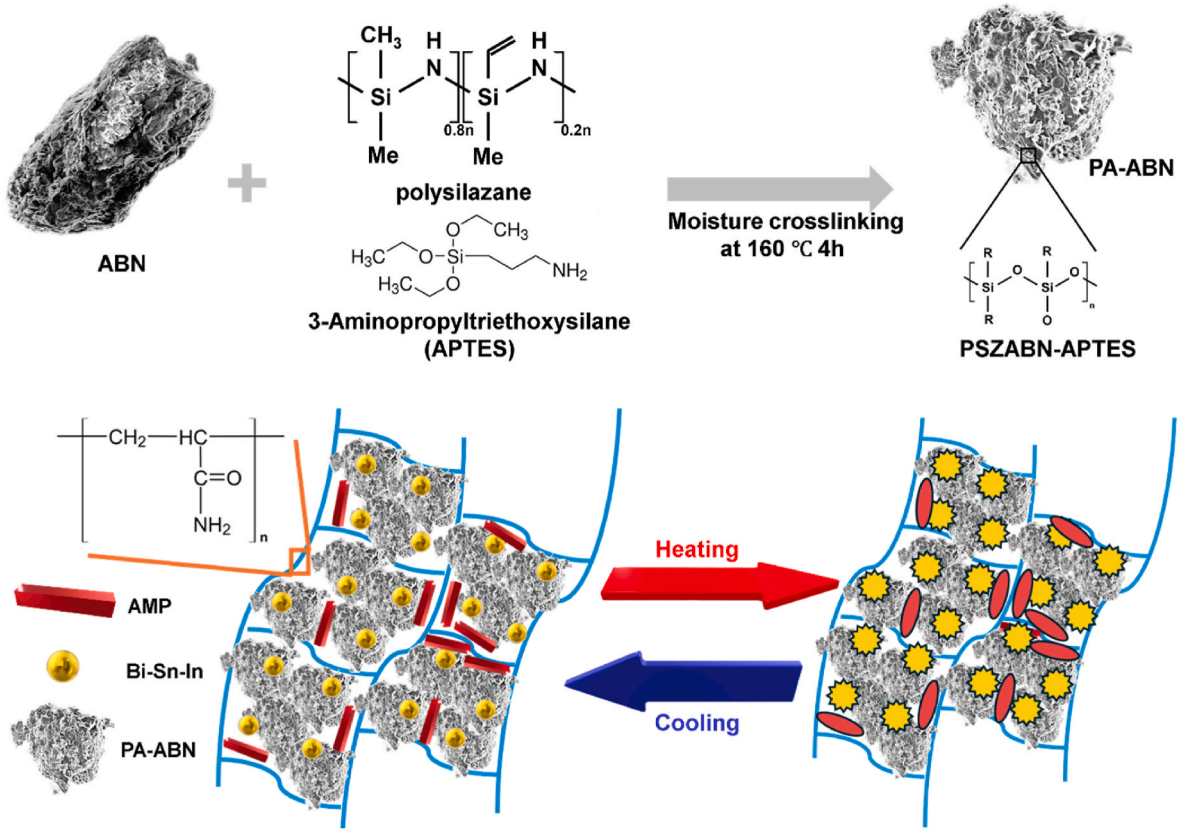


Fig. 1. Schematic illustration of the fabrication process of PA-ABN and the PAM –S/AMP/PA-ABN composites incorporating Bi–Sn–In alloy.

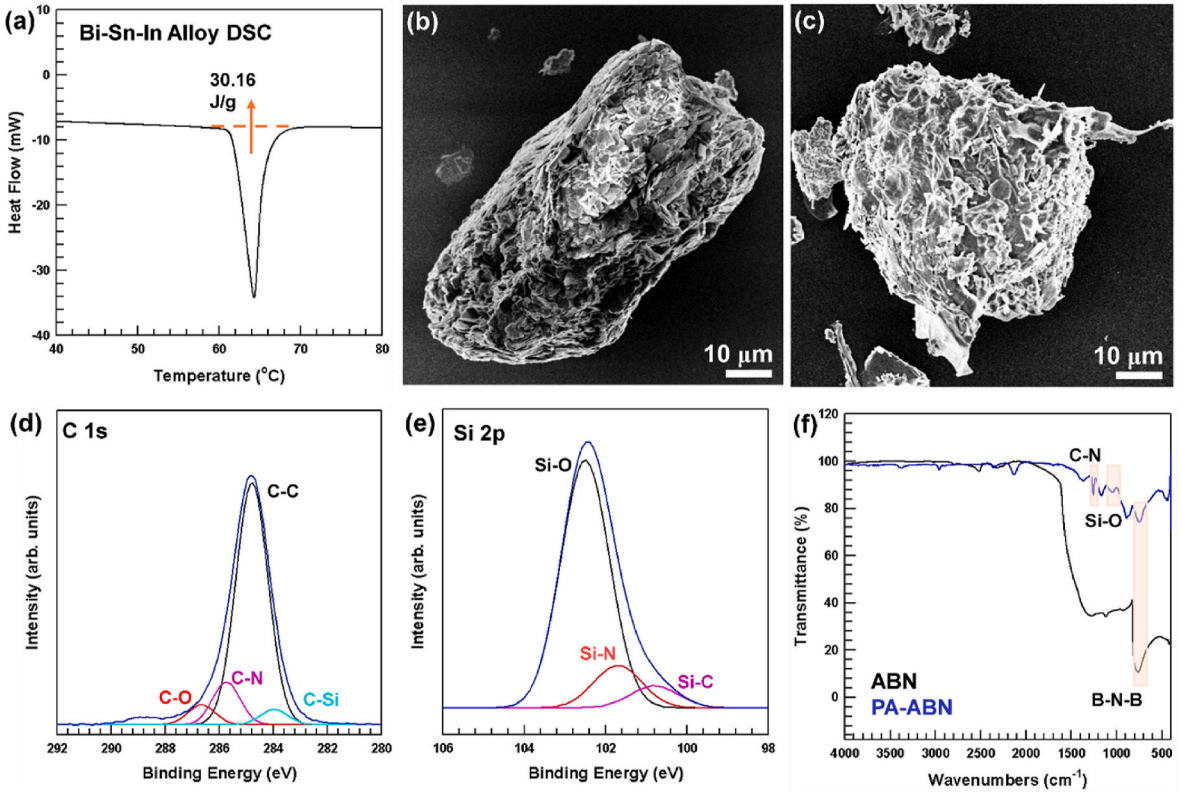


Fig. 2. (a) DSC curve of the Bi–Sn–In alloy. FE–SEM images of (b) ABN and (c) PA-ABN. XPS spectra of (d) C 1s and (e) Si 2p of PA-ABN. (f) FT–IR spectra of ABN and PA-ABN.

Fourier-transform infrared spectroscopy (FT-IR) spectra of surface-modified BN (Fig. 2(f)) exhibited absorption bands at 820 cm^{-1} and 1360 cm^{-1}, corresponding to out-of-plane B–N–B bending vibrations and in-plane B–N stretching vibrations, respectively. The peak observed near 1270 cm^{-1} corresponded to C–N stretching vibrations attributed to the PSZ and APTES structures. Furthermore, the peak near 1070 cm^{-1} was attributed to the formation of Si–O–Si siloxane linkages via hydrolysis and subsequent condensation reactions involving silicon atoms. Thermogravimetric analysis (TGA) of PA-ABN (Fig. S1) was conducted, revealing that ABN exhibited no significant weight loss up to 800 °C under a nitrogen atmosphere, while PA-ABN showed a 15 % weight loss within the same temperature range. This weight loss was attributed to the thermal decomposition of the PSZ and APTES coatings on the ABN surface. Both PSZ and APTES molecules contained oxygen, which reacted with carbon to form CO_2, resulting in mass loss. These findings further confirm the successful surface modification of ABN through PSZ and APTES functionalization.

2.2. Morphological analysis of PAM–S/AMP/PA-ABN composite material

Porous structures are commonly proposed as an effective strategy to prevent PCM leakage. In this study, starch was incorporated during the polymerization of acrylamide to produce a matrix material with a more solid porous structure. Studies show that adding starch during the PAM synthesis enhances the mechanical strength of the porous framework [18]. The FE-SEM image (Fig. 3(a)) revealed that starch particles were attached to the surface of the PAM skeleton, contributing to enhanced mechanical properties. In the absence of starch during PAM synthesis, the resulting solution exhibited low viscosity, similar to that of pure water. This low viscosity enabled the high-density ABN filler to settle, resulting in phase separation. However, when PAM was synthesized with starch, the starch increased the viscosity as the temperature increased, effectively preventing the filler separation. To fabricate PAM–S/AMP/ABN composites, AMP and ABN were incorporated during the synthesis of the PAM porous structure. The detailed procedure is outlined in the Experimental section of the Supporting Information. To achieve a high latent heat, the AMP content was set to 5-fold the weight of PAM. However, the Bi–Sn–In alloy content was fixed at 5 % to prevent electrical insulation loss associated with higher concentrations. Additionally, the high density of the Bi–Sn–In alloy increased the risk of particle sedimentation.

Fig. 3(b–f) illustrates the cross-sectional FE-SEM images of the PAM–S/AMP/ABN composites. During fabrication, AMP was melted in a 100 °C mixed solution of water, acrylamide, and starch, and rapidly cooled to 0 °C in an ice bath before adding ammonium persulfate and N, N′-methylene bisacrylamide. This process induced AMP crystallization within the composites, resulting in the morphology observed in the FE-SEM image (Fig. 3(b)). Compared to the PAM–S/ABN composite, the PAM/ABN composite (without starch) exhibited layer separation between the filler and PAM due to the high density of ABN. Fig. S2 illustrates the optical image of the composites fabricated without starch, clearly revealing the filler separation. The ABN particles settled at the bottom, indicating poor dispersion. In contrast, the PAM-S/ABN composite (Fig. 3(c)) exhibited uniform filler of ABN. The slow precipitation of ABN during the polymerization process, attributed to the increased viscosity induced by starch, allowed the ABN particles to become evenly distributed within PAM-S pores. This uniform filler dispersion contributes to enhanced mechanical strength and thermal conductivity of the composite. However, without surface modification, PAM–S matrix–ABN filler interfacial adhesion was minimal. The cross-sectional FE-SEM image showed that untreated ABN lacked functional groups on its surface, preventing effective interaction with the PAM matrix. Additionally, voids were observed between the PAM–S matrix and the ABN filler, degrading the mechanical and thermal properties of the composite. Surface treatment of ABN enhanced interfacial adhesion with the PAM–S

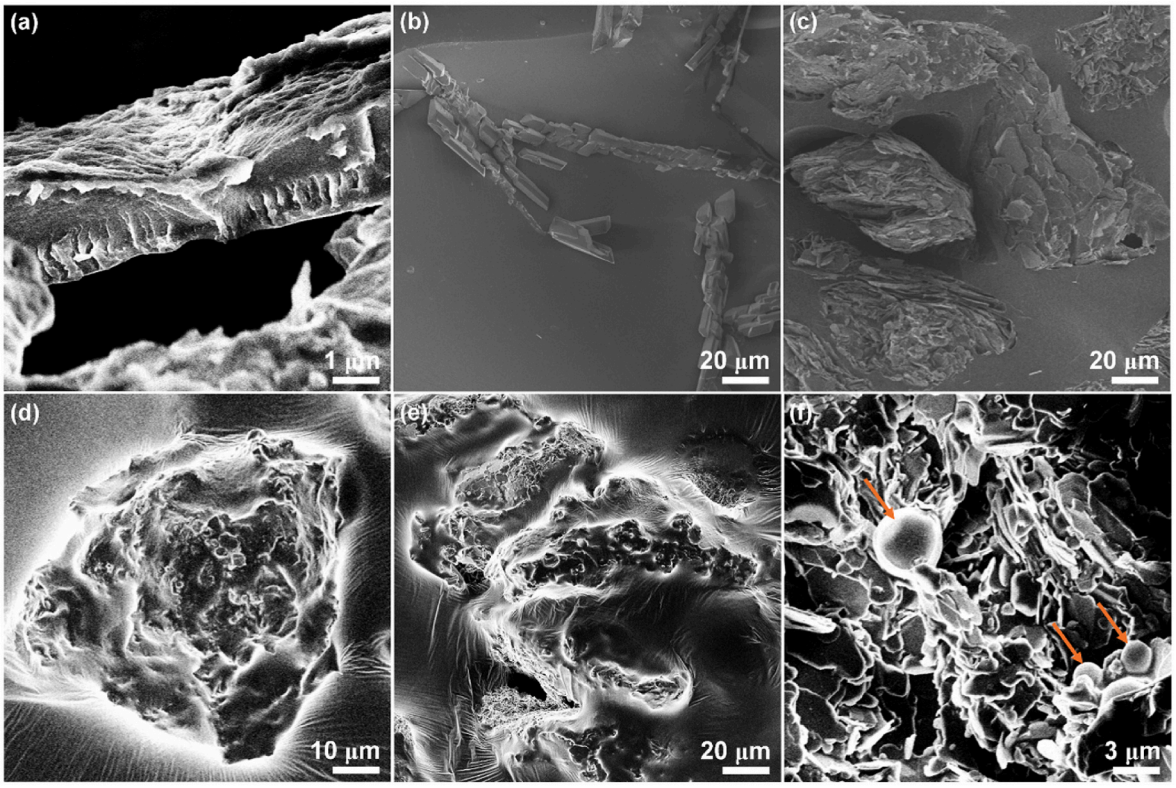


Fig. 3. Cross-sectional FE-SEM images of (a) PAM–S, (b) AMP morphology in the PAM–S/AMP composites, (c) PAM–S/AMP/ABN, (d) PAM–S/AMP/PA-ABN, and (e, f) PAM–S/AMP/PA-ABN composites with Bi–Sn–In particles.

matrix (Fig. 3(d)). When ABN was surface-coated with PSZ and APTES, functional groups formed on its surface, enabling interaction with PAM to create a smooth interface, reducing phonon scattering. Furthermore, the cross-sectional FE-SEM image (Fig. 3(e)) illustrates that the Bi–Sn–In alloy particles, exhibiting high thermal conductivity, effectively filled the PAM pores and the narrow gaps between ABN and PAM, thereby improving the thermal conductivity of the composite. Additionally, some Bi–Sn–In particles exhibited a spherical morphology and were located on the surface of ABN particles. Fig. S3 illustrates that the EDS elemental mapping of the composites revealed the presence of B, N, and Si elements throughout the cross-section, indicating uniform dispersion of the PA-ABN filler. Furthermore, although the Bi–Sn–In alloy content was low, the presence of Bi, Sn, and In elements was still observed.

2.3. Mechanical and thermal properties of PAM–S/AMP/PA-ABN composites

Fig. 4(a) and S4 illustrate the tensile strength of the composites. The pristine PAM matrix exhibited a tensile strength of 2.16 MPa and a high elongation at break of 125 %. After adding starch, the tensile strength increased to 3.13 MPa, while the elongation at break decreased to 110 %. This change is attributed to starch reinforcing the porous structural framework of PAM during synthesis [24]. Additionally, increasing the ABN content increased the tensile strength to 14 MPa and reduced the elongation at break to 50 %. The reduction in tensile strain was attributed to the ABN filler occupying the PAM–S pores, while further improvement in tensile strength was associated with the surface modification of ABN. In composites containing ABN, the decrease in tensile strain is potentially attributed to the filler hindering the mobility of the PAM chains by occupying the porous network of the PAM–S matrix. In contrast, the unfilled PAM/PAM–S matrix deformed due to interconnected pores, facilitating chain movement during tensile testing, with the material being stretched from both ends. This deformation resulted in tensile strains >100 %. However, when the pores were filled with rigid ABN fillers, the surface-treated PA-ABN exhibited enhanced compatibility with the PAM–S matrix, preventing the deformation of the PAM–S chains. This resulted in a significant decrease in tensile strain and a corresponding increase in tensile strength. Fig. S4 shows a schematic illustrating differences between the porous and filler-filled systems during tensile testing.

The thermal conductivity of the composites was measured in the vertical direction at various filler ratios, with Fig. 4(c) illustrating the results. Owing to the porous structure of PAM–S matrix, the thermal conductivity of PAM–S was extremely low, at approximately 0.1 W/m·K. Porous composite materials entrap air, serving as a thermal insulator and thereby reducing thermal conductivity. When the ABN filler ratio in the PAM–S/AMP/PA-ABN composite increased to 30 %, its thermal conductivity reached 3.14 W/m·K, while the PAM–S/AMP/ABN composite exhibited a lower value of 2.67 W/m·K. The higher thermal conductivity of the PAM–S/AMP/PA-ABN composite is attributed to the surface modification with PSZ and APTES, enhancing adhesion between PAM–S and PA-ABN, uniform filler dispersion, and the formation of continuous heat conduction pathways. Furthermore, the composite without starch, PAM/AMP/ABN, exhibited a lower thermal conductivity of 0.44 W/m·K at the same filler ratio than that of the PAM–S/AMP/ABN composite. The cross-sectional FE-SEM image of PAM/ABN synthesized without starch confirmed filler separation, accounting for the reduced thermal conductivity.

For a more accurate prediction, the Lewis–Nielsen model was applied to estimate the thermal conductivity of PAM–S/AMP/PA-ABN composites with varying ABN contents [25,26] with possible fabrication of heat path in Fig. S5. The Lewis–Nielsen model predicts the thermal

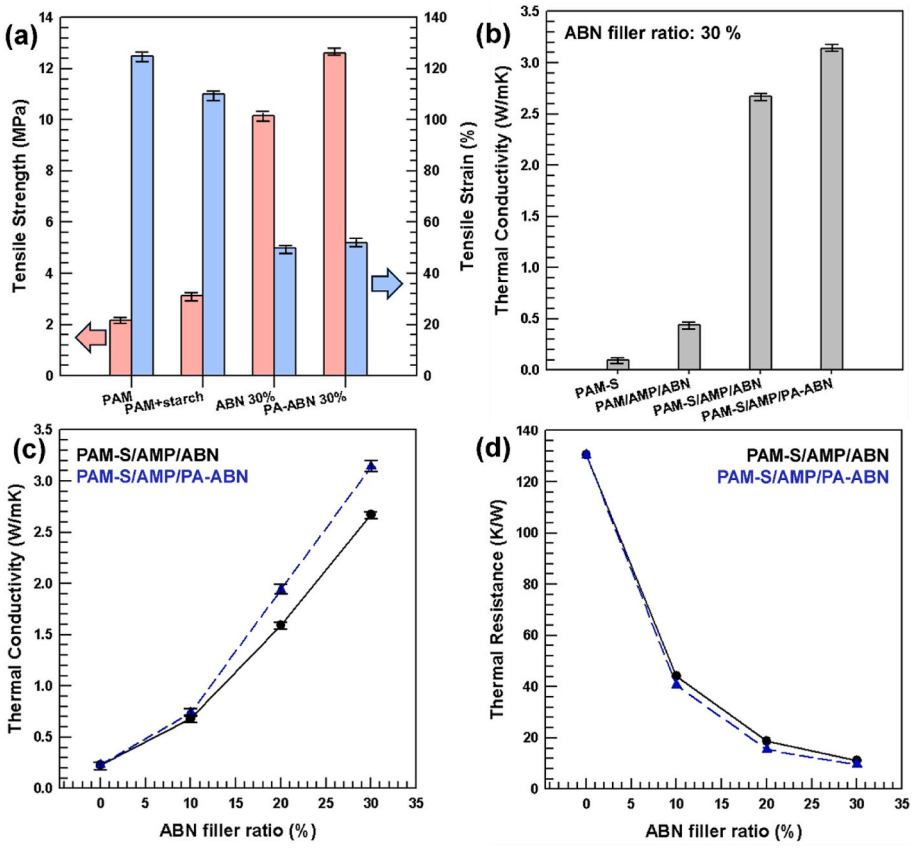


Fig. 4. (a) Tensile strength and strain of PAM–S/AMP/ABN composites. Thermal conductivity of (b) various composites and (c) composites with varying ABN filler content. (d) Thermal resistance of composites with varying ABN filler ratio.

conductivity of polymer composites using Equations (1)–(3):

$$\lambda_c = \lambda_m \frac{1 + \zeta\eta\phi_f}{1 - \Phi\eta\phi_f} \tag{1}$$

$$\eta = \frac{\lambda_f - \lambda_m}{\lambda_f + \zeta\lambda_m} \tag{2}$$

$$\Phi = 1 + \frac{1 - \phi_m}{\phi_m^2}\phi_f\lambda_c\lambda_m \tag{3}$$

where λ_m and λ_f are the thermal conductivities of the PAM–S/AMP matrix and the ABN filler, respectively. ϕ_m and ϕ_f represent the maximum volumetric packing factor of the ABN filler and the volume fraction of ABN filler in the composites, respectively. The ζ is the shape factor of the ABN, accounting for the shape of the filler, primarily its aspect ratio. Equation (2) accounts for the coupling between the conductivities of the matrix and the fillers, along with the geometry of the fillers. The parameter Φ represents the maximum parking fraction of particles potentially incorporated into the polymer matrix. Fig. 4(c) shows the thermal conductivity data fitted using the Lewis–Nielsen model, red dashed line. The fitted results matched the Lewis–Nielsen model predictions up to an ABN filler content of 20 %. However, when the ABN filler content exceeded 30 %, the model showed poor agreement because it does not account for the additional heat transfer pathways at higher filler loadings. The cross-sectional image and schematic of the possible thermal conduction pathways (Fig. S5) show that ABN effectively fills the pores of the PAM–S/AMP matrix, resulting in a high filler volume fraction. This dense network created efficient heat transfer pathways, resulting in a higher thermal conductivity than the value predicted by the model.

The PAM–S/AMP/PA-ABN composite containing 5 % Bi–Sn–In alloy exhibited the highest thermal conductivity (3.34 W/m·K) because the alloy filled the PAM–S–PA-ABN filler interstitial spaces and pores, while exhibiting inherently high thermal conductivity. However, the volumetric fraction of the Bi–Sn–In alloy should remain minimal to achieve this enhancement in thermal conductivity. However, the volumetric fraction of the Bi–Sn–In alloy was minimal and did not significantly affect the improvement of thermal conductivity. When electrical insulation was not considered a limiting factor, the Bi–Sn–In content was further increased to improve thermal conductivity. This improvement was further confirmed using the calculated thermal resistance (Fig. 4 (d)). PAM–S/AMP composites exhibited a porous structure containing various pores, resulting in high thermal resistance. Incorporating fillers filled these pores and established continuous heat transfer pathways, thereby reducing the thermal resistance of the composite.

Fig. 5 illustrates the latent heat values of the PAM–S/AMP/ABN composites. Pure AMP exhibits a high latent heat of 256 J/g, demonstrating two distinct peaks [27]. The primary melting point of AMP occurs at 110 °C, while the peak observed at 90 °C corresponds to its solid–solid phase transition. DSC analysis revealed that the latent heat associated with the solid–solid phase transition below the melting point was 231 J/g, indicating that high latent heat can be maintained in applications below 100 °C without a solid–liquid phase change. When AMP was incorporated into the PAM–S matrix at varying ratios, with Fig. 5(b & C) showing the corresponding latent heat values. Increasing the AMP content enhanced the solid–solid phase change latent heat, reaching 198 J/g at a PAM–S:AMP weight ratio of 1:5. The high latent heat in this system is due to the efficient encapsulation of AMP within the interconnected pores of the starch-reinforced PAM-S matrix, minimizing PCM loss and preserving phase-change capacity. Mechanistically, the porous PAM-S framework reinforced with starch plays a crucial role in stabilizing AMP crystals and preventing filler precipitation during the synthesis process. Starch increases matrix viscosity at high temperatures, enabling uniform distribution of AMP and mitigating segregation. This uniform dispersion allows the AMP to maintain its crystallinity during thermal cycling, preserving its characteristic DSC properties. As the ABN filler content increased, the latent heat of the composites decreased to 138 J/g within the 70–90 °C range. In general, adding fillers to organic PCM matrices reduces their latent heat storage capacity. However, incorporating a porous filler structure and forming a continuous filler network within the matrix significant mitigated these losses, thereby maintaining latent heat performance. Mechanistically, the porous PAM-S framework reinforced with starch plays a crucial role

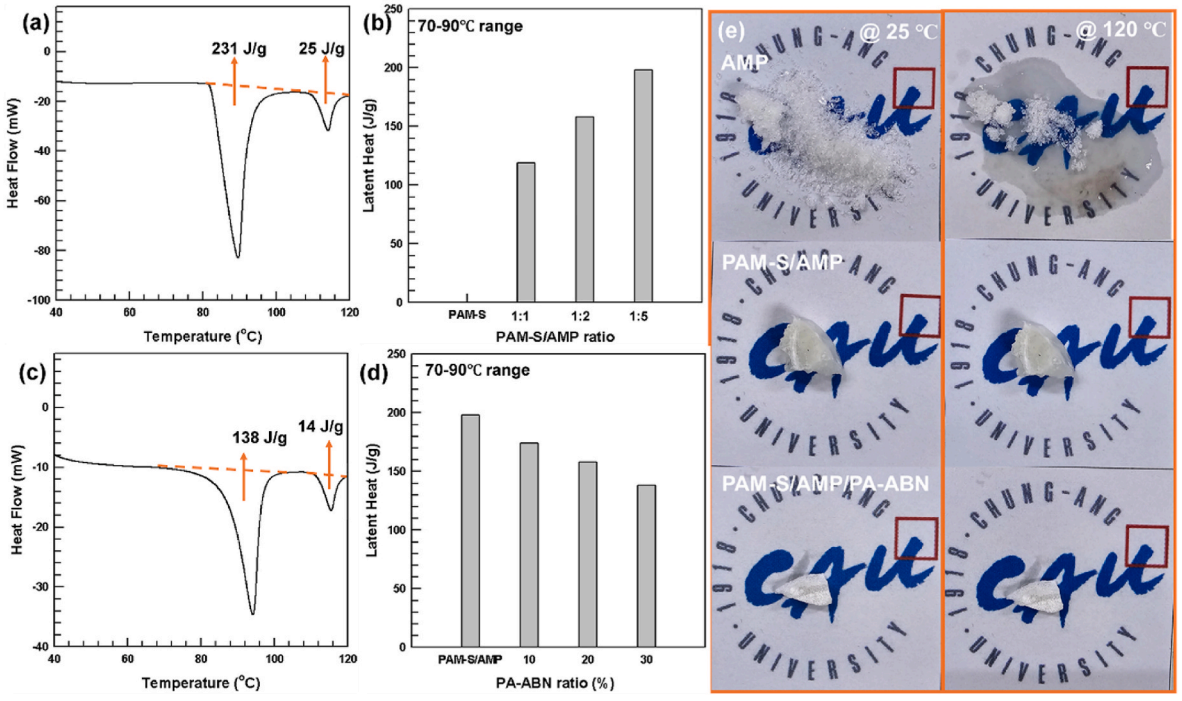


Fig. 5. (a) DSC curve of pristine AMP. (b) Calculated latent heat at different PAM–S/AMP ratios. (c) DSC curve of PAM–S/AMP containing 30 % PA-ABN. (d) Latent heat of composites with varying PA-ABN ratios.

in stabilizing AMP crystals and preventing filler precipitation during the synthesis process. Starch increases matrix viscosity at high temperatures, enabling uniform distribution of AMP and mitigating segregation. This uniform dispersion allows the AMP to maintain its crystallinity during thermal cycling, preserving its characteristic DSC properties. Also, the hybrid filler partially occupies the pore space, limiting the AMP volume expansion/contraction during the solid-solid transition. This combined effect of porous structural confinement, starch-induced viscosity control, and hybrid filler thermal networking can not only maintain high latent heat but also enhance thermal conductivity (3.34 W/m K). Leakage tests revealed that the prepared composites exhibited significantly enhanced structural stability under heat (Fig. 5(e)). Pure AMP melted at 120 °C, while PAM–S/AMP and PAM–S/AMP/PA-ABN composites exhibited no signs of leakage. This finding suggests that AMP is effectively trapped within the porous PAM–S structure, demonstrating the ability of the matrix to prevent PCM leakage.

Compared to recent literature, our composites shows high latent heat with high thermal conductivity. A direct comparison is difficult because the latent heat of PCMs varies depending on the melting point and material. However, due to the low thermal conductivity of the PCM material, materials with high latent heats typically have low thermal conductivity. However, due to the synergistic effect of the porous PAM-S network and the hybrid filler, we were able to simultaneously achieve a high latent heat of 138 J/g and a high thermal conductivity of 3.34 W/m•K (Table 1).

Fig. 6(a and b) shows the results of thermal cycling tests conducted to assess the thermal stability and reliability of the PAM–S/AMP/PA-ABN composite. After 100 thermal cycles, the latent heat changed by only 5 %, with no measurable mass loss, indicating that the composite exhibited excellent thermal stability and reliability. Prior to the application tests, TGA analysis was performed on the PAM–S/AMP/PA-ABN composite to further confirm its thermal stability (Fig. 6(c)). The composite exhibited no significant mass loss up to 140 °C. Beyond this temperature, the organic compound reacted with the oxygen atoms, leading to decomposition and subsequent mass loss, leaving approximately 50 % of the original mass. These findings indicate that the composite maintains thermal stability below 140 °C, making it suitable for heat dissipation and temperature control in electronic devices. Due to the structural advantages explained above, the composites can maintain thermal stability over 100 cycles.

Fig. 7 illustrates the application of PAM–S/AMP/PA-ABN composites to a working CPU to evaluate its heat dissipation performance. The composites, PAM–S/AMP and PAM–S/AMP/PA-ABN, were used as TIMs between the CPU and the heat sink. The thermal behavior was examined under operational conditions (Fig. 7(b and c)). The PAM–S/AMP/PA-ABN composite exhibited the most effective thermal management, demonstrating the lowest peak temperature and the slowest temperature increase compared to both the PAM–S/AMP composite and the CPU without thermal paste. The infrared thermal images confirmed these findings, showing that the PAM–S/AMP/PA-ABN-applied CPU exhibited a brighter central region, indicating more effective heat spreading and dissipation to the surroundings. This effect is attributed to the continuous through-plane thermal conduction network formed by the aligned PA-ABN fillers within the PAM–S/AMP matrix, facilitating rapid heat transfer away from the CPU core. Additionally, the PAM–S/AMP/PA-ABN composite exhibited a latent heat capacity of 138 J/g, enabling its significant thermal energy storage during phase transition temperature fluctuation stabilization. Consequently, both the heating and cooling curves progressed more gradually than those of the bare CPU, clearly demonstrating the inherent thermal buffering capacity of the PCM. This dual mechanism—high thermal conductivity for efficient steady-state dissipation below the melting point, and latent heat storage for transient load buffering above the melting point—enhanced thermal stability during CPU operation. Overall, integrating PAM–S/AMP/PA-ABN composite as a thermal interface material offers superior control of CPU temperature profiles, thereby extending safe operational duration and reducing the risk of thermal shock compared to conventional thermal interface materials. During practical CPU operation, the PAM–S/AMP/PA-ABN sample exhibited both a slower temperature increase and a lower peak temperature than both the PAM–S/AMP sample and the CPU without thermal paste. Specifically, the rate of temperature increase over time exhibited a pattern consistent with the phase transition region of the PCM, indicating that latent heat absorption is crucial during this stage. This performance enhancement is attributed to the formation of effective heat-transfer pathways via the aligned ABN structure within the PAM–S/AMP matrix, facilitating through-plane thermal conductivity. These high-conductivity channels accelerate heat transfer to the PCM regions, enabling rapid latent heat storage and improving the overall thermal buffering capacity.

Table 1
Thermal energy storage and thermal conductivity properties comparison in literature.

Composites	Melting point (°C)	Latent Heat (J/g)	Thermal Conductivity (W/m•K)	Ref.
FSPCM	61.3	131.63	–	[28]
PG/ExG-4 %	82	163.8	0.863	[29]
PG/GP/CNT	80.5	145.6	–	[30]
SSPCM-3	65.3	158.2	0.478	[31]
BPPCM-2	57	104	1.22	[32]
FPCM85	57.4	157.4	–	[33]
HPCM	28	27	0.52	[34]
SSWPC-30	29.9	17.5	–	[35]
FRPCM2	47	91	1.05	[36]
PAM–S/AMP/PA-ABN containing 5 % Bi-Sn-In alloys	90	138	3.34	This work

3. Conclusion

This study demonstrates a novel PCM composite architecture that integrates a reinforced PAM–S framework, PA-ABN, and a Bi–Sn–In liquid metal alloy to simultaneously address three key challenges in PCM-based thermal management: leakage prevention, thermal transport efficiency, and mechanical robustness. The optimized composite exhibited a through-plane thermal conductivity of 3.34 W/m•K, tensile strength of 14 MPa, and latent heat capacity of 138 J/g, while effectively preventing leakage up to 120 °C. The material maintained >95 % of its latent heat capacity after 100 thermal cycles, demonstrating excellent long-term stability and reliability under repeated operation. CPU cooling tests further confirmed that the composite lowers peak operating temperatures and slows temperature rise rates, validating its practical application as a high-performance thermal interface material.

Beyond the performance metrics, the synergistic design—integrating a mechanically reinforced porous network, surface-engineered thermally conductive fillers, and microvoid-infiltrating liquid metal—offers a novel materials engineering pathway for electrically insulating PCM systems. The findings demonstrate that interfacial optimization combined with hybrid filler integration can mitigate the inherent trade-offs among thermal conductivity, phase-change capacity, and leakage resistance that limit conventional PCM composites.

However, this study has some limitations. The filler content was restricted by the requirement to maintain electrical insulation, while the Bi–Sn–In alloy fraction must be minimized to prevent density-induced segregation. Additionally, while short-term cycling stability was verified, performance under long-term cycling beyond 1000 cycles, high-humidity exposure, and mechanical fatigue from thermal expansion was not evaluated. Therefore, future studies should focus on optimizing filler architectures to enhance conductivity without compromising phase-change capacity, developing scalable fabrication methods, and conducting accelerated aging tests to assess long-term performance in real-world applications.

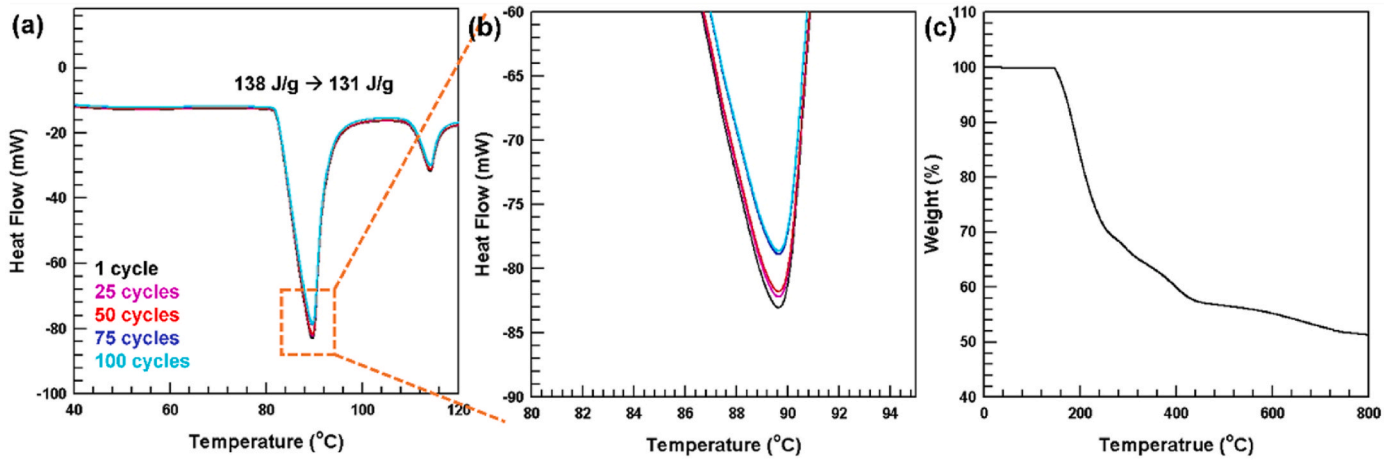


Fig. 6. (a) DSC curves after 100 thermal cycling tests. (b) high resolution DSC curves for orange box in Fig. 6(a). (c) TGA results for PAM–S/AMP/ABN composites.

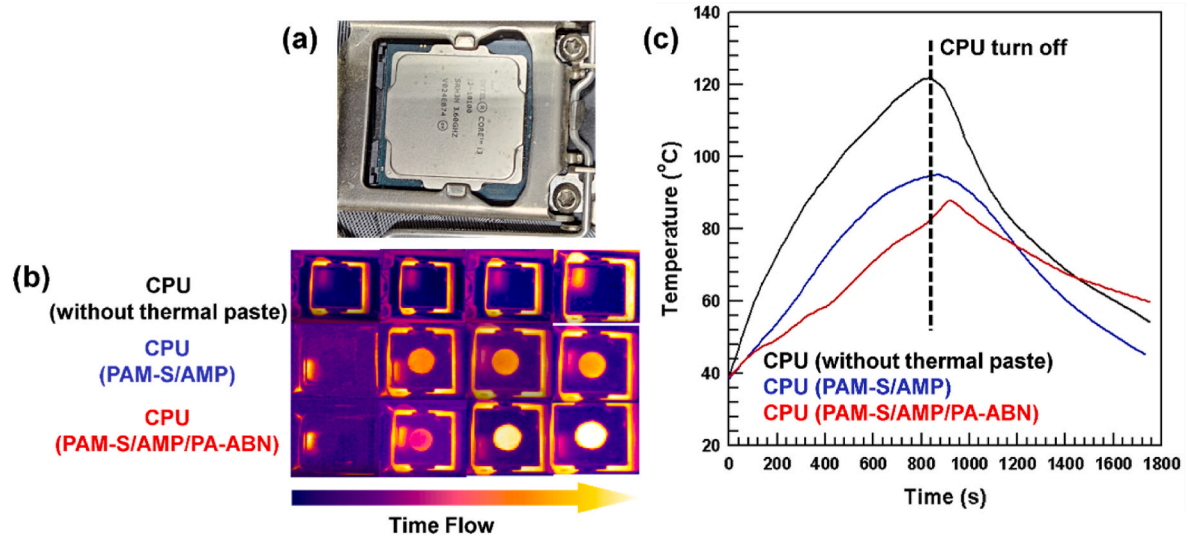


Fig. 7. (a) Used CPU image from computer. (b) IR thermal image of CPU with composites, (c) thermal management comparison on CPU using composites.

Overall, this study contributes to the field of PCM-based thermal management by presenting a robust, multifunctional composite that integrates high latent heat storage, enhanced heat dissipation, and superior structural stability, facilitating next-generation energy storage and electronic cooling applications.

CRediT authorship contribution statement

Minsu Kim: Writing – original draft, Investigation, Formal analysis, Data curation, Conceptualization. **Dabin Park:** Investigation, Conceptualization. **Jooheon Kim:** Supervision, Project administration, Funding acquisition.

Declaration of competing interest

The authors declare that they have no known competing financial interests or personal relationships that could have appeared to influence the work reported in this paper.

Acknowledgement

This work was supported by Korea Institute of Energy Technology Evaluation and Planning (KETEP) grant funded by the Korea government (MOTIE) RS-2024-00398346, ESS BigData-Based O&M and Asset Management Technical Manpower Training) and the National Research Foundation of Korea (NRF) grant funded by the Korea government (MSIT) (NRF-2022M3H4A1A02076956).

Appendix A. Supplementary data

Supplementary data to this article can be found online at https://doi.org/10.1016/j.polymertesting.2025.108963.

Data availability

Data will be made available on request.

References

[1] Z. Said, A.K. Pandey, A.K. Tiwari, B. Kalidasan, F. Jamil, A.K. Thakur, V. Tyagi, A. Sarı, H.M. Ali, Nano-enhanced phase change materials: fundamentals and applications, Prog. Energy Combust. Sci. 104 (2024) 101162.
[2] V.R. Jagadeeswara, M.F. Ghazali, S. Kumarasamy, Advancements in phase change materials for energy-efficient building construction: a comprehensive review, J. Energy Storage 81 (2024) 110494.
[3] H. Togun, H.S. Sultan, H.I. Mohammed, A.M. Sadeq, N. Biswas, H.A. Hasan, R. Z. Homod, A.H. Abdulkadhim, Z.M. Yaseen, P. Talebizadehsardari, A critical review on phase change materials (PCM) based heat exchanger: different hybrid techniques for the enhancement, J. Energy Storage 79 (2024) 109840.

[4] M. Farid, A.M. Khudhair, S.A.K. Razack, S. Al-Hallaj, A review on phase change energy storage: materials and applications, Thermal Energy Storage Phase Change Mater. (2021) 4–23.
[5] W. Aftab, A. Usman, J. Shi, K. Yuan, M. Qin, R. Zou, Phase change material-integrated latent heat storage systems for sustainable energy solutions, Energy Environ. Sci. 14 (2021) 4268–4291.
[6] R. Cai, Z. Sun, H. Yu, E. Meng, J. Wang, M. Dai, Review on optimization of phase change parameters in phase change material building envelopes, J. Build. Eng. 35 (2021) 101979.
[7] Y. Gao, X. Meng, A comprehensive review of integrating phase change materials in building bricks: methods, performance and applications, J. Energy Storage 62 (2023) 106913.
[8] A.K. SR, S. Sivan, V.C. Midhun, S.R. Behera, Experimental and numerical investigation of solid-solid phase change material assisted heat sink with integrated heat pipe for electronic cooling, J. Energy Storage 59 (2023) 106494.
[9] G. Righetti, C. Zilio, L. Doretti, G.A. Longo, S. Mancin, On the design of phase change materials based thermal management systems for electronics cooling, Appl. Therm. Eng. 196 (2021) 117276.
[10] H. Chen, A. Abidi, A.K. Hussein, O. Younis, M. Degani, B. Heidarshenas, Investigation of the use of extended surfaces in paraffin wax phase change material in thermal management of a cylindrical lithium-ion battery: applicable in the aerospace industry, J. Energy Storage 45 (2022) 103685.
[11] F. Wang, D. Pang, X. Liu, M. Liu, W. Du, Y. Zhang, X. Cheng, Progress in application of phase-change materials to cooling clothing, J. Energy Storage 60 (2023) 106606.
[12] K. Yan, Y. Feng, L. Qiu, Thermal and photo/electro-thermal conversion characteristics of high energy storage density expanded graphite/polyethylene glycol shaped composite phase change materials, Sol. Energy 272 (2024) 112477.
[13] R.K. Rajamony, B. Kalidasan, A.G.N. Sofiah, Y.A. Bhutto, S.K. Suraparaju, A. K. Pandey, J.K. Siaw Paw, M.S. El-Sebaey, Engineering of thermal energy storage: an experimental study of organic/silver and organic/silver-coconut shell biochar composite phase change materials, Therm. Sci. Eng. Prog. 62 (2025) 103639.
[14] T. Bo, T. Zhi-Cheng, L. Rui-Bin, M. Chang-Gong, Z. Jing-Nan, Thermodynamic investigation of a solid–solid phase change material: 2-amino-2-methyl-1,3-propanediol by calorimetric methods, Energy Convers. Manag. 51 (2010) 1905–1910.
[15] L. Fan, J.M. Khodadadi, Thermal conductivity enhancement of phase change materials for thermal energy storage: a review, Renew. Sustain. Energy Rev. 15 (2011) 24–46.
[16] P. Cheng, X. Chen, H. Gao, X. Zhang, Z. Tang, A. Li, G. Wang, Different dimensional nanoadditives for thermal conductivity enhancement of phase change materials: fundamentals and applications, Nano Energy 85 (2021) 105948.
[17] D. Zhao, M. Feng, L. Zhang, B. He, X. Chen, J. Sun, Facile synthesis of self-healing and layered sodium alginate/polyacrylamide hydrogel promoted by dynamic hydrogen bond, Carbohydr. Polym. 256 (2021) 117580.
[18] X. Mu, J. Zhou, P. Wang, H. Chen, T. Yang, S. Chen, L. Miao, T. Mori, A robust starch–polyacrylamide hydrogel with scavenging energy harvesting capacity for efficient solar thermoelectricity–freshwater cogeneration, Energy Environ. Sci. 15 (2022) 3388–3399.
[19] K. Chen, J. Ding, W. Wang, J. Lu, Shape-stable Bi-Sn-In alloy/Ag/copper foam composite phase change material for thermal storage and management, Chem. Eng. J. 454 (2023) 140087.
[20] S. Ki, S. Shin, S. Cho, S. Bang, D. Choi, Y. Nam, Sustainable thermal regulation of electronics via mitigated supercooling of porous gallium-based phase change materials, Adv. Sci. 11 (23) (2024) 2310185.
[21] Z. Hanif, K.-I. Choi, J.-H. Jung, A.G.M. Pornea, E. Park, J. Cha, H.-R. Kim, J.-H. Choi, J. Kim, Dispersion enhancement of boron nitride nanotubes in a wide range of solvents using plant polyphenol-based surface modification, Ind. Eng. Chem. Res. 62 (2023) 2662–2670.
[22] W. Yan, X. Chen, J.S.K. Lim, H. Chen, V. Gill, A. Lambourne, X. Hu, Epoxy-assisted ball milling of boron nitride towards thermally conductive impregnable composites, Compos. Appl. Sci. Manuf. 156 (2022) 106868.
[23] K. Kim, H. Ju, J. Kim, Pyrolysis behavior of polysilazane and polysilazane-coated-boron nitride for high thermal conductive composite, Compos. Sci. Technol. 141 (2017) 1–7.
[24] H. Taghavian, S.-O. Ranaei-Siadat, M.R. Kalaee, S. Mazinani, Investigation of the effects of starch on the physical and biological properties of polyacrylamide (PAAm)/starch nanofibers, Prog. Biomater. 6 (2017) 85–96.
[25] J. Czyzewski, A. Rybak, K. Gaska, R. Sekula, C. Kapusta, Modelling of effective thermal conductivity of composites filled with core-shell fillers, Materials 13 (23) (2020) 5480.
[26] H. Song, B.G. Kim, Y.S. Kim, Y.-S. Bae, J. Kim, Y. Yoo, Synergistic effects of various ceramic fillers on thermally conductive polyimide composite films and their model predictions, Polymers 11 (3) (2019) 484.
[27] R. Gotoh, T. Totani, M. Wakita, H. Nagata, Controlling heat release of crystallization from supercooling state of a solid-solid PCM, 2-amino-2-methyl-1,3-propanediol, Int. J. Heat Mass Tran. 137 (2019) 1132–1140.
[28] C. Chen, W. Liu, Z. Wang, K. Peng, W. Pan, Q. Xie, Novel form stable phase change materials based on the composites of polyethylene glycol/polymeric solid-solid phase change material, Sol. Energy Mater. Sol. Cell. 134 (2015) 80–88.
[29] N. Zhang, Y. Song, Y. Du, Y. Yuan, G. Xiao, Y. Gui, A novel solid–solid phase change material: Pentaglycerine/Expanded graphite composite PCMs, Adv. Eng. Mater. 20 (10) (2018) 1800237.
[30] Q. Xiao, Y. Xu, X. Li, H. Tang, H. Li, L. Zhang, Enhanced solar-thermal and electro-thermal storage performance of solid-solid composite phase change material, Compos. Commun. 45 (2024) 101818.
[31] Y. Xia, H. Zhang, P. Huang, C. Huang, F. Xu, Y. Zou, H. Chu, E. Yan, L. Sun, Graphene-oxide-induced lamellar structures used to fabricate novel composite solid-solid phase change materials for thermal energy storage, Chem. Eng. J. 362 (2019) 909–920.
[32] C. Tian, Y. Yang, Q. Liu, Y. Bai, F. Zhao, L. Huang, N. yang, X. Cai, W. Kong, Molecular regulation of flexible composite solid–solid phase change materials with controllable isotropic thermal conductivity for thermal energy storage, ACS Appl. Mater. Interfaces 15 (10) (2023) 13165–13175.
[33] Z. Liu, B. Wu, X. Fu, P. Yan, Y. Yuan, C. Zhou, J. Lei, Two components based polyethylene glycol/thermosetting solid-solid phase change material composites as novel form stable phase change materials for flexible thermal energy storage application, Sol. Energy Mater. Sol. Cell. 170 (2017) 197–204.
[34] T. Harlé, R.L. Hebert, G.T.M. Nguyen, B.A. Ledésert, A composite of cross-linked polyurethane as solid–solid phase change material and plaster for building application, Energy Build. 262 (2022) 111945.
[35] X. Guo, H. Jiang, C. Qiu, T. Lu, R. Wei, M. Fan, Y. Zhang, W. Sun, An energy storage composite using cellulose grafted polyethylene glycol as solid–solid phase change material, Polym. Compos. 45 (2) (2024) 1524–1533.
[36] T. Wu, P. Chen, Z. Zhang, Z. Wu, Y. Hu, S. Cai, C. Wang, Synergistically flame-retardant solid-solid phase change composites for battery thermal safety systems, Appl. Therm. Eng. 279 (2025) 127637. Part B.